

Reduced upwelling of nutrient and carbon-rich water in the subarctic Pacific during the Mid-Pleistocene Transition

Savannah Worne^{1*}, Sev Kender^{2,3,*}, George E. A. Swann¹, Melanie J. Leng^{3,4}, and Ana Christina Ravelo⁵

¹Centre for Environmental Geochemistry, School of Geography, University of Nottingham, Nottingham, NG7 2RD, UK.

²Camborne School of Mines, University of Exeter, Penryn Campus, Penryn, Cornwall, TR10 9FE, UK (s.kender@exeter.ac.uk)

³National Environmental Isotope Facility, British Geological Survey, Keyworth, Nottingham, NG12 5GG, UK

⁴Centre for Environmental Geochemistry, School of Biosciences, University of Nottingham, Sutton Bonington Campus, Loughborough, NE12 5RD, UK

⁵University of California, Santa Cruz, CA 95064, USA

*Corresponding authors

Contact: Savannah Worne (savannah.worne@nottingham.ac.uk); Sev Kender (s.kender@exeter.ac.uk); George Swann (george.swann@nottingham.ac.uk); Melanie Leng (mjl@bgs.ac.uk) and Ana Christina Ravelo (acr@ucsc.edu)

Key words: MPT; Sea Ice; CO₂; Bering Sea; Upwelling index

Abstract

Reduction in atmospheric $p\text{CO}_2$ has been hypothesised as a causal mechanism for the Mid-Pleistocene Transition (MPT), which saw global cooling and increased duration of glacials between 0.6 and 1.2 Ma. Sea ice-modulated high latitude upwelling and ocean-atmospheric CO₂ flux is considered a potential mechanism for $p\text{CO}_2$ decline, although there are no long-term nutrient upwelling records from high latitude regions to test this hypothesis. Using nitrogen isotopes and opal mass accumulation rates from 0 to 1.2 Ma, we calculate a continuous high resolution nutrient upwelling index for the Bering Sea and assess possible changes to regional CO₂ fluxes and to the relative control of sea ice, sea level and North Pacific Intermediate Water (NPIW) on deep mixing and nutrient upwelling in the region. We find nutrient upwelling in the Bering Sea correlates with global ice volume and air temperature throughout the study interval. From ~1 Ma, and particularly during the 900 ka event, suppressed nutrient upwelling would have lowered oceanic fluxes of CO₂ to the atmosphere supporting a reduction in global $p\text{CO}_2$ during the MPT. This timing is consistent with a pronounced increase in sea ice during the early Pleistocene and restriction of flow through the Bering Strait during glacials after ~ 900 ka, both of which would have acted to suppress upwelling. We suggest that sea-level modulated NPIW expansion during glacials after 900 ka was the dominant control on subarctic Pacific upwelling strength during the mid-late Pleistocene, while sea ice variability played a secondary role.

43 1. Introduction

44 The Mid-Pleistocene Transition (MPT) occurred between ~1.2 and 0.6 Ma when glacial-
45 interglacial cycles in global climate increased from a 41 kyr to a longer quasi-100 kyr periodicity
46 (McClymont et al., 2013). The MPT centres on a step-wise increase in benthic foraminiferal $\delta^{18}\text{O}$
47 at the “900 ka event” (~ 0.9 Ma), characterised by a dramatic increase in continental ice sheet
48 volume and resultant rapid declines in global sea level (~50 to 200 m) during post-MPT glacial
49 periods when 100 kyr cyclicity emerges (Lisiecki & Raymo, 2005; Elderfield et al., 2012) together
50 with changes in thermohaline circulation (Schmieder et al., 2000; Sexton & Barker, 2012).
51 Proposed mechanisms for MPT climate evolution include changing land ice-sheet dynamics (Clark
52 & Pollard, 1998; Raymo et al., 2006; Crowley & Hyde, 2008), either controlled by basal erosion
53 or continental ice-sheet instability following expansion of the Antarctic ice sheet (Clark et al.,
54 2006; Pollard & DeConto, 2009). Alternatively, the MPT may represent a tipping point in a long-
55 term decrease in atmospheric $p\text{CO}_2$ (Raymo, 1997; Hönlisch et al., 2009) and/or an alteration in
56 ocean-atmosphere CO_2 exchange (Pena & Goldstein, 2014), particularly from high latitude oceans
57 as a result of increased stratification and/or increased efficiency of the biological pump following
58 altered nutrient/dust supply (McClymont et al., 2008; Martinez-Garcia et al., 2010; Martínez-
59 Garcia et al., 2011; Rodríguez-Sanz et al., 2012; Chalk et al., 2017; Kender et al., 2018). Others
60 have suggested that a shift in the moisture balance and resultant relationship between northern
61 hemispheric sea ice and land ice formation (the “sea ice switch”) following deep ocean cooling
62 could also have been key (Gildor & Tziperman, 2001).

63
64 These hypotheses remain largely untested partly due to a lack of high resolution and long-term
65 palaeoenvironmental data. Despite increasing evidence for changing ocean/atmosphere interaction
66 in the high latitudes and atmospheric teleconnection with lower latitudes following ice-sheet
67 expansion in the mid-late Pleistocene (Marlow et al., 2000; Heslop et al., 2002; Liu & Herbert,
68 2004; McClymont & Rosell-Melé, 2005; McClymont et al., 2008; Sexton & Barker, 2012), it is
69 not clear whether these feedbacks were sufficient to control climate change and cause increased
70 ice volumes and/or decreased atmospheric $p\text{CO}_2$. Modelling and observational evidence is also
71 biased towards the Southern Ocean, a critical region for the growth of land and sea ice, deep water
72 formation and the upwelling of nutrient- and CO_2 -rich waters, fuelling an efficient but variable
73 biological pump that dominates atmospheric CO_2 variability over Quaternary glacial-interglacial
74 cycles (Billups et al., 2018).

75
76 Another key, but comparatively understudied location is the high latitude subarctic Pacific
77 Ocean and the Bering Sea, which is adjacent to the North American Ice Sheets (NAIS) and has
78 been influenced by sea ice since the onset of Northern Hemispheric glaciation (~2.6 Ma) (Teraishi
79 et al., 2016; Stroynowski et al., 2017). The Bering Sea, bounded to the north by the Bering Strait
80 which connects the Pacific and Arctic Oceans (Stabeno et al., 1999), is a region of
81 palaeoceanographic importance as nutrient- and carbon-rich North Pacific Deep Water (NPDW)
82 upwells at the Bering shelf. The upwelling and vertical mixing of NPDW, driven by eddies and

83 instabilities in the shelf-adjacent Bering Slope Current (BSC), results in seasonally high photic
84 zone $p\text{CO}_2$ and primary productivity along the Bering slope (Figure 1). Understanding the long-
85 term changes in subarctic Pacific upwelling, in addition to the Southern Ocean, is therefore
86 important to test the hypothesis that high latitude upwelling contributed to a change in atmospheric
87 CO_2 during the MPT.

88
89 Previous research from the Bering slope has shown a strong link between NPDW upwelling at
90 the shelf edge and global atmospheric $p\text{CO}_2$ in the mid-late Pleistocene (0 to 0.85 Ma), with
91 expanded sea ice suggested to modulate deep water upwelling and ocean-atmosphere CO_2
92 exchanges across the wider subarctic Pacific region (Kender et al., 2018; Worne et al., 2019). This
93 process is suggested to result from increased sea ice and restriction of flow through the Bering
94 Strait due to lower sea level during glacials, hereafter referred to as ‘closure of the Bering Strait’,
95 promoting the expansion of dense and macronutrient poor North Pacific Intermediate Water
96 (NPIW) across the subarctic Pacific region. Today, NPIW is widely distributed across the North
97 Pacific Ocean at a water depth between ~300 – 800 m (Talley, 1993) and is characterised as a
98 salinity minima with a density centred at $26.8 \sigma_\theta$ (Yasuda, 1997). Although NPIW is currently
99 sourced primarily from the Okhotsk Sea, there is evidence that indicates the Bering Sea was a key
100 source of NPIW during past glacials (Horikawa et al., 2010; Ohkushi et al., 2003) as a result of
101 enhanced brine rejection on the Beringian shelf, following increased sea ice growth since ~900
102 kyr (Kender et al., 2018; Knudson & Ravelo, 2015). Expansion of NPIW during post-MPT glacials
103 would have prevented NPDW upwelling and causing region-wide isolation of CO_2 in deep waters
104 (Knudson & Ravelo, 2015b; Kender et al., 2018; Worne et al., 2019).

105
106 However, the short temporal resolution of these existing MPT records from the Bering Sea,
107 and the lack of similar datasets from the early Pleistocene, limit an assessment of the relationship
108 between global climate, atmospheric $p\text{CO}_2$ and subarctic nutrient upwelling, prior to significant
109 glacial sea level decline at 0.9 Ma when the Bering Strait first closed (Kender et al., 2018). Here,
110 we present the first continuous nutrient upwelling index (Worne et al., 2019) from the Bering Sea
111 slope from 1.2 Ma onwards . With this, we aim to determine the long-term evolution of nutrient
112 upwelling and its significance for the wider subarctic Pacific Ocean and the global atmospheric
113 $p\text{CO}_2$ changes hypothesised to control climate cooling during the MPT (Raymo, 1997; Hönisch et
114 al., 2009).

115 **2. Materials and methods**

116 **2.1. Core materials**

117 Sediment cores from IODP Site U1343 (57°33.39'N, 175°48.95'W, water depth 1,950 m) were
118 collected during IODP Expedition 323. Situated on a topographic high adjacent to the northern
119 continental shelf, and proximal to the modern winter sea ice edge, IODP Site U1343 sits in the
120 high productivity green belt region, which is directly influenced by high eddy activity in the shelf-
121 adjacent BSC, which facilitates high rates of nutrient upwelling and stimulates primary
122 productivity (Figure 1). Marine sediments are composed primarily of fine clays and biogenic
123 material, and are characteristically distinct from shelf-transported materials (Takahashi et al.,
124 2011; Aiello & Ravelo, 2012).

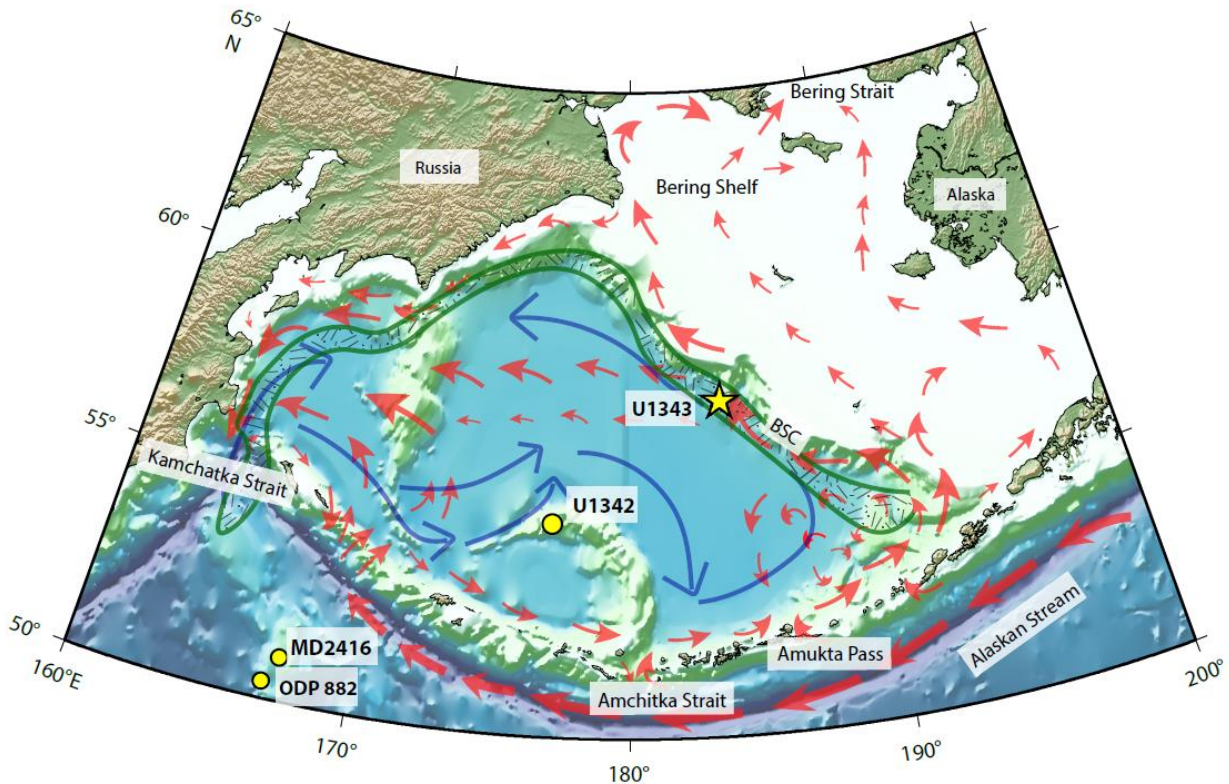


Figure 1 The geographical location and oceanography of the Bering Sea (adapted from Worne et al., (2019)). The white area represents the continental shelf region to the north and the blue represents the Bering Basin. Yellow dots indicate sites of previous important palaeoceanographic study through the Pleistocene including Site ODP 882 and MD2416 from the western subarctic Pacific and IODP Site U1342 from the Southern Bering Sea. Site U1343 (this study) is marked by a yellow star. Surface water circulation is marked by red arrows, which flow in from the Alaskan Stream and through various straits and passes in the Aleutian island arc. Surface water circulates in an anti-clockwise gyre, where turbulence and eddies in the shelf adjacent Bering Slope Current (BSC) causes a high productivity region known as the green belt, represented by the green patterned shape (Springer et al., 1996). Deep water circulation is marked by blue arrows, entering from the lower subarctic Pacific Ocean through the deep western Kamchatka Strait.

125

126 2.2. Site U1343: updated age model (1.014 – 1.2 Ma)

127 Good preservation of benthic foraminifera at Site U1343 has allowed construction of a high
128 resolution $\delta^{18}\text{O}$ age model from 0 to 0.85 Ma (1.1 kyr resolution; Worne et al., 2019) and from
129 0.85 to 1.02 Ma (0.22 kyr resolution; Kender et al., 2018). Here we present 48 new benthic $\delta^{18}\text{O}$
130 data points from 1.02 to 1.20 Ma (284.06 – 338.32 m CCSF-A), to extend the age model back to

131 1.2 Ma. Following previous studies at this site, ~100 μg of foraminiferal calcite from four species
132 (*Elphidium batialis*, *Globobulimina auriculata*, *Islandiella norcrossi* and *Uvigerina bifurcate*)
133 were measured for $\delta^{18}\text{O}$, applying species-specific offsets previously defined at Site U1343
134 (Kender et al., 2018) to fit the data to the most commonly occurring species, *E. batialis*. The $\delta^{18}\text{O}$
135 measurements were made using an IsoPrime 100 dual inlet mass spectrometer with a Multicarb
136 device at the National Environmental Isotope Facility, British Geological Survey. Results are
137 calculated relative to the VPDB scale using within-run laboratory standard (KCM, $\delta^{18}\text{O} = -1.73\text{‰}$)
138 that has been calibrated using the international reference material NBS 19 ($\delta^{18}\text{O} = -2.20\text{‰}$). The
139 KCM standard had an analytical reproducibility of $<0.05\text{‰}$ ($\pm 1\sigma$, $n = 94$). We combine all existing
140 records to produce a composite $\delta^{18}\text{O}$ record of 1,825 data points, with an average resolution of
141 0.65 kyr on an updated age model (Figure 2; Supplementary Table 1).

142

143 **2.3. Bulk sedimentary $\delta^{15}\text{N}$**

144 Bulk sedimentary $\delta^{15}\text{N}$ was previously published for Site U1343 ($\delta^{15}\text{N}_{\text{U1343}}$) between 0 to 0.85
145 Ma (Kim et al., 2017; Worne et al., 2019) and 0.85 to 1.02 Ma (Kender et al., 2018). Here we
146 present 62 new bulk sediment $\delta^{15}\text{N}_{\text{U1343}}$ data points between 1.02 to 1.20 Ma (284.06 – 338.32 m
147 CCSF-A). These were measured using 50 mg of raw material on a Carlo Erba 1108 elemental
148 analyzer, interfaced to a Thermo Finnigan Delta Plus XP IRMS at the University of California,
149 Santa Cruz, with a precision of 0.15‰ based on duplicates. Stable isotope data were calibrated
150 using Pugel standard (mean $\delta^{15}\text{N} = +5.48\text{‰}$, $\sigma = 0.16$), with additional in-house long term quality
151 controlled through comparison with sediments from IODP Site U1342 in the southern Bering Sea
152 (mean $\delta^{15}\text{N} = +2.89\text{‰}$, $\sigma = 0.19$). We combine all existing records to produce a composite $\delta^{15}\text{N}_{\text{U1343}}$
153 record of 623 data points, with an average resolution of 1.9 kyr on the updated age model.

154

155 **2.4. Nutrient upwelling index**

156 The bulk $\delta^{15}\text{N}_{\text{U1343}}$ record in the Bering Sea has been suggested to be influenced by a
157 denitrification signal which propagates from the Eastern Tropical North Pacific (ETNP) (Brunelle
158 et al., 2007). Therefore, we follow previous work (Galbraith et al., 2008; Knudson & Ravelo,
159 2015a; Worne et al., 2019) subtracting North Pacific Ocean $\delta^{15}\text{N}$ records from ODP Site 1012 in
160 the eastern tropical North Pacific Ocean ($\delta^{15}\text{N}_{1012}$), thought to be a site of complete nutrient
161 utilisation as well as being influenced by waters originating from the ETNP denitrification zone
162 (Liu et al., 2005; Galbraith et al., 2008). By constraining for background changes in source water
163 ($\delta^{15}\text{N}_{1012}$), the resultant isotope record ($\delta^{15}\text{N}_{\text{U1343-1012}}$) predominantly reflects changes in nutrient
164 utilisation at the Bering slope (Worne et al., 2019).

165

166 As nutrient utilisation is a product of both the total nutrient supply (predominantly from
167 upwelling along the slope) and biogenic productivity, the opal MAR records from Site U1343

168 (Kim et al., 2014) can be used to further constrain the $\delta^{15}\text{N}_{\text{U1343-1012}}$ record, following the
169 methodology of Worne et al., (2019) in which the opal MAR and $\Delta\delta^{15}\text{N}_{\text{U1343-1012}}$ are normalised:
170

$$171 \quad \text{Nutrient Upwelling Index} = \text{Normalised Opal MAR} - \text{Normalised } \Delta\delta^{15}\text{N}_{\text{U1343-1012}} \quad (1)$$

172
173 The resultant calculation is termed the nutrient upwelling index (Eq. 1), in which we
174 assume that the upwelling of NPDW was the dominant supply of macronutrients to surface waters
175 at Site U1343, and that rates of nutrient utilisation are controlled by both upwelling strength and
176 the delivery of iron (Fe) from sea ice entrained sources (in addition to contributions from deep
177 water and potential minor inputs from volcanic sources). Given that the green belt is iron limited
178 (Aguilar-Islas et al., 2007; Takeda, 2011), under a constant rate of nutrient upwelling Fe supply
179 will increase both productivity and nutrient utilisation and will therefore not change the nutrient
180 upwelling index significantly (Worne et al., 2019). Therefore, the resultant “nutrient upwelling
181 index”, is a semi-quantitative measure of nutrient supply, where low (high) values suggest a
182 decrease (increase) in NPDW upwelling strength at the Bering slope.
183

184 **3. Results**

185 **3.1. Age model**

186 The extended Site U1343 benthic foraminiferal $\delta^{18}\text{O}_{\text{U1343}}$ record contains 1,825 data points
187 with a mean time step of 0.65 kyr between 0 and 1.2 Ma. The age model was defined by correlating
188 to the LR04 global composite stack (Lisiecki & Raymo, 2005), choosing 30 age-depth tie points
189 at periods of rapid isotopic change (e.g. deglacials) (Figure 2, Supplementary Table 1). Poor linear
190 regression between foraminiferal $\delta^{13}\text{C}$ and raw $\delta^{18}\text{O}$ ($r = 0.43$, $p < 0.01$) shows that diagenetic
191 alteration of foraminiferal shells does not explain the glacial-interglacial variability in the benthic
192 foraminiferal $\delta^{18}\text{O}$ isotope data at Site U1343 (Asahi et al., 2016; Kender et al., 2018; Worne et
193 al., 2019; Detlef et al., 2020).

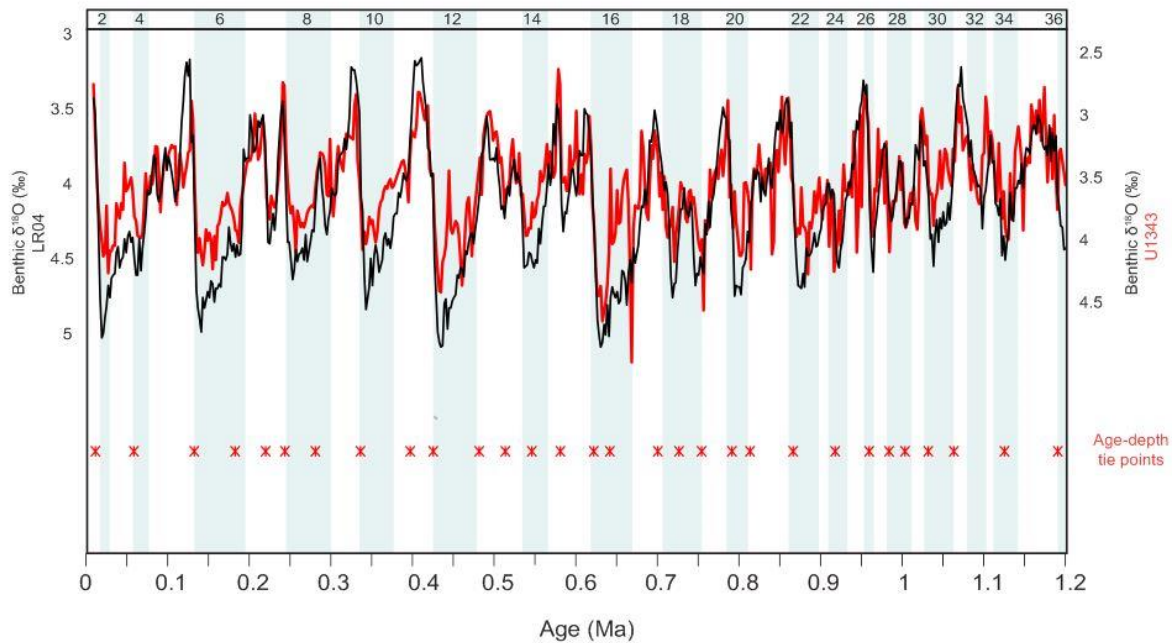


Figure 2 Age Model for Site U1343 from MIS 2 to 36. Benthic foraminiferal $\delta^{18}\text{O}$ results from IODP Site U1343 (red) compared to the LR04 global benthic $\delta^{18}\text{O}$ stack (black) (Lisiecki & Raymo, 2005), with blue bars represent glacial periods. Age-depth tie points used to tune the age model for Site U1343 with the LR04 stack are shown as red crosses (Supplementary Table 1).

195 3.2. $\delta^{15}\text{N}_{\text{U1343}}$ and the nutrient upwelling index

196 Pre-MPT $\delta^{15}\text{N}_{\text{U1343}}$ results show a higher mean (1.02 to 1.20 Ma; mean = +6.6‰) than during
197 the 900 ka event (~0.85 to 0.95 Ma; mean = +6.0‰) or post-MPT (0 to 0.85 Ma; mean = +5.6‰)
198 (Figure 3A). This is consistent with higher opal MAR during this period, where increased
199 productivity caused a larger proportion of the $\delta^{15}\text{N}$ inferred nutrient pool to be used. The exception
200 to this occurs during MIS 34 when opal MAR is low and $\delta^{15}\text{N}_{\text{U1343}}$ is high, leading the low
201 upwelling index values. Low opal MAR during this glacial is unlikely to be a result of opal
202 dissolution, as silica diagenesis is not prevalent in the cores at Site U1343 (Takahashi et al., 2011),
203 confirmed by good preservation of diatoms down-core (Teraishi et al., 2016). Therefore, low
204 upwelling index results at MIS 34 are most likely the result of increased sea ice and a highly
205 fluctuating sea ice margin during the build up to MPT conditions (Detlef et al., 2018) (see Section
206 4.2).

207 There is also glacial-interglacial variability in $\delta^{15}\text{N}_{\text{U1343}}$ with glacials exhibiting significantly
208 lower nutrient utilisation (mean = +5.7‰) than interglacial periods (mean = +5.9‰, $p < 0.05$), co-
209 occurring with higher productivity during warmer periods (Figure 3A). The exception to this
210 occurs at the MIS 31/32 boundary (~1.06 Ma) when nutrient utilisation is notably low, although
211 there is no notable change in lithology or biogenic composition of the sediment (Takahashi et al.,
212 2011).

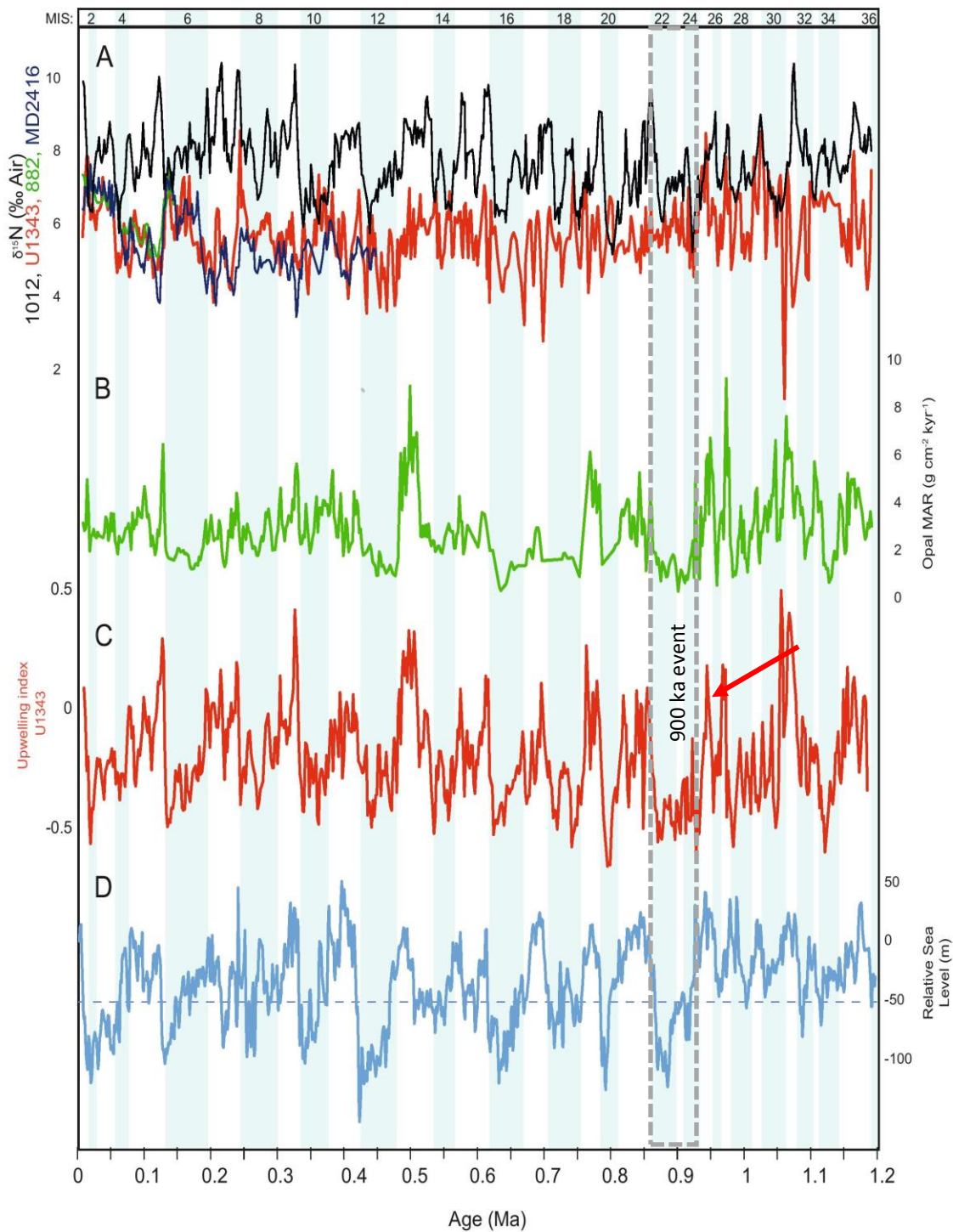


Figure 3 Geochemical proxy results from IODP Site U1343 from MIS 2 to 36. A) Bulk $\delta^{15}\text{N}$ data from IODP Site U1343 compared with deep North Pacific ODP Site 1012 (a site of complete nutrient utilisation) (black) together with records from ODP Site 882 (green) and MD2416 (navy blue) in the subarctic Pacific Ocean. B) Opal mass accumulation rate (MAR) from IODP Site U1343 (Kim et al., 2014). C) Upwelling index between 0 – 1.2 Ma (red) are compared to D) relative sea level estimates from Elderfield et al., (2012), where the dashed line represents a 50 m sea level decline, below which the Bering Strait was likely closed. Blue shaded bars represent glacial periods as defined by the LR04 benthic stack (Lisiecki & Raymo, 2005), with a grey dashed line to represent the 900 ka event.

215 From MIS 33 (~1.12 Ma) the nutrient upwelling index shows a gradual increase, reaching a
216 peak in early glacial MIS 30 (~1.05 Ma), where productivity is high and nutrient utilisation is
217 minimal (Figure 3C). Between MIS 30 and MIS 28 (~1.05 to 0.98 Ma), results show a sharp and
218 continued decrease in nutrient upwelling as colder MPT conditions develop (global composite
219 benthic $\delta^{18}\text{O}$, Figure 2), with interglacial upwelling remaining low during MIS 29 (~1.02 Ma).
220 Despite a recovery in nutrient upwelling strength through MIS 27 – 25 (~0.97 to 0.93 Ma),
221 particularly in interglacials where both productivity (opal MAR) and the rate of nutrient utilisation
222 ($\delta^{15}\text{N}_{\text{U1343}}$) are notably high, a rapid decline in the upwelling index occurs during MIS 24 (~0.91
223 Ma) where productivity is minimal (Figure 3A-C). During the 900 ka event, there is a continued
224 minima in nutrient upwelling index values, particularly through MIS 23 and early MIS 22 (~0.86
225 to 0.91). At the end of glacial MIS 22 there is a gradual increase in nutrient upwelling strength and
226 recovering productivity towards the deglacial peak. From MIS 21 (~0.85 Ma) onwards, nutrient
227 upwelling exhibits strong glacial-interglacial variability, with low upwelling during glacials and
228 high upwelling during interglacials (Worne et al., 2019).

229
230 Although $\delta^{15}\text{N}_{\text{U1343}}$ excursions may also be a result of variable inorganic or terrestrial input,
231 a lack of glacial-interglacial covariation between $\delta^{15}\text{N}_{\text{U1343}}$ and C/N suggests inorganic nitrogen
232 input does not have an overriding control on $\delta^{15}\text{N}_{\text{U1343}}$ (Kim et al., 2017; Worne et al., 2019).
233 Furthermore, low $\delta^{15}\text{N}$ values measured at more distal open ocean subarctic Pacific sites, e.g. Site
234 MD2416, ODP Site 882 (Figure 1) and ODP Site 887, together with diatom-bound $\delta^{15}\text{N}$ values of
235 less than 5‰ at IODP Site U1343 (Kim & Khim, 2016), provides confidence that nutrient
236 utilisation changes rather than terrestrial/inorganic nitrogen input, is the most significant control
237 on Quaternary glacial-interglacial $\delta^{15}\text{N}_{\text{U1343}}$ variability.

238

239 4. Discussion

240 4.1. Nutrient upwelling and glacial-interglacial CO_2 (0.85 – 1.20 Ma)

241 The upwelling index from 0 – 0.85 Ma has been previously shown to correlate with a number
242 of proxy and modelled climate records (Worne et al., 2019), including the LR04 deep ocean $\delta^{18}\text{O}$
243 record (Lisiecki & Raymo, 2005), relative sea level changes (Elderfield et al., 2012), global surface
244 ocean temperatures (Snyder, 2016) and Antarctic air temperatures (Jouzel et al., 2007). In
245 particular, a strong correlation with global benthic $\delta^{18}\text{O}$ and $p\text{CO}_2$ (Lüthi et al., 2008) ($r = 0.60$, p
246 < 0.001), was suggested to indicate a common underlying mechanism between NPDW upwelling
247 in the Bering Sea and global climate changes (Worne et al., 2019). Over the extended 0 – 1.2 Ma
248 interval presented here, a strong correlation is maintained between the upwelling index and relative
249 sea level ($r = -0.49$, $p < 0.001$), surface air temperatures ($r = 0.58$, $p < 0.001$), and particularly the
250 LR04 stack ($r = -0.66$, $p < 0.001$). This is consistent with the hypothesis that subarctic Pacific
251 upwelling was integral to the climate system during the MPT (Kender et al., 2018). Although the
252 age model for the upwelling index was tuned to the LR04 stack, the high resolution of the dataset
253 (2 kyr) and the limited number of tie points used (30; Figure 2, Supplementary Table 1), suggests

254 that the relationship between global ice volume, surface ocean temperature and Bering Sea nutrient
255 upwelling is not an age-model artefact.

256

257 Given the link between upwelling subarctic Pacific Ocean deep water and deglacial
258 atmospheric CO₂ ventilation for the last deglaciation (Rae et al., 2014; Gray et al., 2018),
259 hypotheses that invoke a reduction in atmospheric *p*CO₂ to drive cooling during the MPT (Raymo,
260 1997; Hönlisch et al., 2009) can be partially tested by examining the evolution of subarctic Pacific
261 upwelling in the build up to the MPT. The upwelling index at Site U1343 shows a long-term glacial
262 fall from ~1.1 to 0.9 Ma (arrow in Figure 3C), which is in line with the hypothesis that the supply
263 of subarctic Pacific CO₂ ventilation to the atmosphere decreased during this interval (Kender et al.
264 2018), and is consistent with CO₂ acting as a driver of MPT climate. While there is no continuous
265 *p*CO₂ proxy record through the MPT for direct comparison, δ¹¹B inferred *p*CO₂ reconstruction
266 from ODP Site 990 in the Caribbean Sea (Chalk et al., 2017) and ODP Site 668B in the eastern
267 equatorial Atlantic (Hönlisch et al., 2009), are not inconsistent with the upwelling index during the
268 early Pleistocene (Figure 4B), with higher nutrient upwelling and *p*CO₂ occurring during warmer
269 interglacial periods. Despite an offset between *p*CO₂ and nutrient upwelling minima in MIS 34,
270 the subsequent increase in *p*CO₂ is consistent with increasing nutrient upwelling. Further support
271 for the correlation between nutrient upwelling in the Bering Sea and global *p*CO₂ is found in the
272 predicted *p*CO₂ record from the CYCLOPS carbon cycle model (Chalk et al., 2017) (Figure 4C).
273 The only sustained discrepancy between the two datasets appears during the 900 ka event, when
274 nutrient upwelling remains lower than predicted CYCLOPS *p*CO₂, particularly during late MIS 22
275 (Figure 4C), coincident with a sustained global sea level drop of >50 m (Elderfield et al., 2012;
276 Kender et al., 2018) (Figure 3D). However, as *p*CO₂ records do not exist in high resolution over
277 the MPT, there is a need for more CO₂ proxy data to confirm the nutrient upwelling link with
278 atmospheric *p*CO₂ at that time.

279

280 **4.2. Long-term sea ice controls on Bering Sea nutrient upwelling**

281 Our record demonstrate a consistent relationship between Bering Sea nutrient upwelling and
282 global climate (LR04 benthic stack), with reduced subarctic Pacific upwelling coincident with
283 falling atmospheric CO₂ which has been suggested to have caused MPT cooling (Raymo, 1997;
284 Hönlisch et al., 2009; Pena & Goldstein, 2014) and/or an alteration in ocean-atmosphere CO₂
285 exchange. Although this correlation does not prove that reduced subarctic Pacific upwelling caused
286 the MPT, it does support a common mechanism which links subarctic high latitude upwelling with
287 atmospheric *p*CO₂, which subsequently would have contributed to global climate changes through
288 the MPT (Kender et al., 2018; Worne et al., 2019). Previous studies have proposed glacial
289 expansion of NPIW across the subarctic Pacific as the linking mechanism to suppress upwelling
290 and regional CO₂ leakage to the atmosphere (Kender et al., 2018; Worne et al., 2019). However
291 variable rates of nutrient utilisation prior to 0.9 Ma, as well as higher glacial sea levels which
292 would not restrict Bering Strait flow (and hence prevent NPIW formation), suggests be an

293 additional control on nutrient upwelling prior to the 900 ka event, in addition to or instead of NPIW
294 formation.

295 Glacial-interglacial variability in Bering Sea upwelling index after 0.9 Ma is also suggested
296 to be influenced by sea ice as a secondary control (Worne et al., 2019). Seasonal sea ice cycling
297 plays an active role in controlling total annual primary production (opal MAR) through stabilising
298 the water column and supplying micronutrients, which in turn facilitates a spring melt associated
299 bloom (Aguilar-Islas et al., 2008; Kanematsu et al., 2013). The size of the subsequent
300 summer/autumn bloom is then highly dependent on the degree of post-melt stratification and the
301 availability of remaining nutrients after drawdown in the spring (Hansell et al., 1989), which in
302 turn influences the annual rate of nutrient utilisation ($\delta^{15}\text{N}_{\text{U1343}}$) (Kender et al., 2018; Worne et al.,
303 2019). Diatom evidence from the Bering slope indicates that sea ice began to expand through both
304 glacials and interglacials from at least ~1 Ma (Teraishi et al., 2016; Stroynowski et al., 2017; Detlef

305 et al., 2018), when sea ice seasons became more prominent in the build up to the 900 ka event.
306 Therefore, we suggest that increased seasonal sea ice and greater fluctuations in the location and
307 duration of sea ice margin caused higher frequency variability in nutrient upwelling strength and
308 acted as the dominant control on the upwelling index at the Bering slope prior to the 900 ka event.
309 This is in contrast to conditions after 0.9 Ma, when closure of the Bering Strait and increased sea
310 ice during the 900 ka event caused glacial formation of NPIW, which became the dominant control
311 on nutrient upwelling. Higher resolution sea ice reconstruction work is required to fully resolve

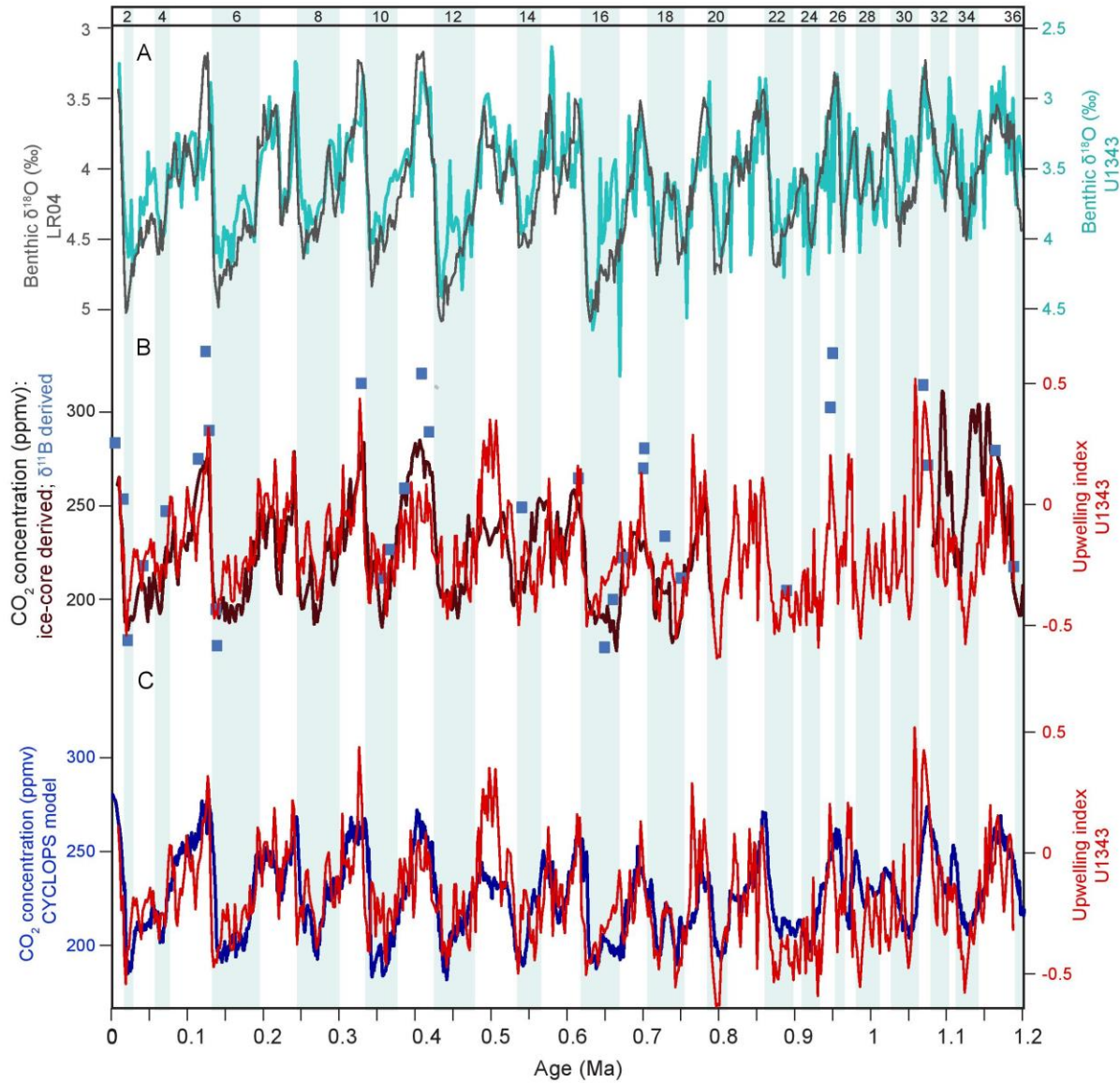


Figure 4 Upwelling index dataset for Site U1343 compared to global climate and $p\text{CO}_2$ reconstructions. A) Benthic foraminifera $\delta^{18}\text{O}$ from Site U1343 (red) and the LR04 benthic stack (black). b) Upwelling index between 0 to 1.2 Ma (red) are compared to $p\text{CO}_2$ (black) from the Vostok ice core between 0 to 0.8 Ma (Lüthi et al., 2008), and $\delta^{11}\text{B}$ between ~1.07 to 1.2 Ma (Chalk et al., 2017). Low resolution boron isotope-derived $p\text{CO}_2$ estimates from Hönisch et al. (2009) are also displayed as light blue squares. C) Comparison of the Bering Sea upwelling index results (red) with modelled atmospheric CO₂ concentrations (dark blue) (Chalk et al., 2017).

312 the relationship between deep water upwelling and sea ice dynamics in the early and middle
313 Pleistocene.

314 **4.3. Long-term sea level and NPIW control on regional subarctic Pacific Ocean upwelling**

315 Although sea ice dynamics were likely important for determining primary productivity and
316 nutrient utilisation rates at the Bering slope in the build up to the 900 ka event, this does not
317 preclude the hypothesis that NPIW had a dominant influence on nutrient upwelling during and/or
318 after the MPT in the subarctic Pacific. For example, Knudson & Ravelo, (2015b) find evidence for
319 NPIW in the southern Bering Sea (Site U1342; Figure 1) back to at least 1.2 Ma. During the 900
320 ka event, when significant land ice accumulated, sea level declined by more than 50 m and caused
321 probable closure of the Bering Strait (Elderfield et al., 2012; Kender et al., 2018). Diatom evidence
322 also suggests that a prolonged pack ice cover occurred during this peak MPT period (Teraishi et
323 al., 2016; Stroynowski et al., 2017). The coincidence of persistent sea ice cover and Bering Strait
324 closure with suppression of nutrient upwelling through MIS 23 up to the end of MIS 22, supports
325 the idea that NPIW expansion and enhanced stratification resulted in reduced vertical mixing of
326 nutrient-rich waters across the region (Kender et al., 2018). Therefore, the upwelling index
327 supports the notion that retention of CO₂ in the deep subarctic Pacific, potentially together with
328 changes in the Southern Ocean (Sigman et al., 2010), was an important mechanism in sustaining
329 low subarctic Pacific upwelling, and reducing regional leakage of CO₂ to the atmosphere during
330 the MPT which ultimately promoted longer glacial periods and larger glacial ice sheets due to its
331 cooling effect (Kender et al., 2018).

332
333 After the 900 ka event, strong glacial-interglacial variability in the nutrient upwelling index
334 developed, which has been interpreted to reflect continued control of glacially enhanced sea ice
335 and NPIW formation on nutrient upwelling in the Bering Sea, causing both a reduced
336 summer/autumn bloom season and acting as a physical barrier to deep water upwelling at the
337 Bering Sea slope (Worne et al., 2019). The establishment of clear glacial-interglacial variability in
338 nutrient utilisation ($\delta^{15}\text{N}_{\text{U1343}}$), despite reduced magnitude of opal MAR variability, indicates that
339 the size of the nutrient pool varied, at least partially, independently from primary productivity (and
340 hence seasonality of the sea ice margin) (Figure 3). Indeed, Worne et al., (2019) noted that the
341 correlation between nutrient upwelling and global $p\text{CO}_2$ was particularly strong over the last 0.35
342 Ma. Therefore, we propose that the glacial expansion of NPIW (reducing the size of the subsurface
343 nutrient pool) would have continued to act as the first-order control on nutrient upwelling after the
344 MPT (Worne et al., 2019), following trends in global climate and $p\text{CO}_2$.

345 346 **5. Conclusions**

347 In summary, we find reduced subarctic nutrient upwelling over the MPT, which would have
348 acted to lower atmospheric $p\text{CO}_2$. We hypothesise that this contributed to global cooling before
349 and during the 900 ka event, possibly alongside changes in other upwelling regions such as the
350 Southern Ocean, by reducing CO₂. However, existing $p\text{CO}_2$ estimates are of too low resolution to

351 resolve if lower levels coincided with the MPT. During the early Pleistocene, evidence exists for
352 increased Bering Sea sea ice extent, but a highly fluctuating sea ice margin between MIS 28 and
353 24 can account for the high frequency variability in nutrient upwelling found in our records. During
354 the 900 ka event, where our nutrient upwelling index is at its lowest for the whole record (0 to 1.2
355 Ma), accumulation of continental ice sheets and severe sea level decline may have facilitated thick
356 pack ice cover in the Bering Sea. When combined with a closure of the Bering Strait, this likely
357 caused an expansion of a strong NPIW, layer which suppressed nutrient upwelling at the Bering
358 Slope. Southward propagation of this NPIW, and reduced regional-scale vertical mixing/deep
359 water ventilation in the subarctic Pacific Ocean, could then have potentially contributed to lower
360 global $p\text{CO}_2$ and ultimately a failure of the interglacial at MIS 23 to result in a full deglacial (Kender
361 et al., 2018)(Kender et al., 2018)(Kender et al., 2018)(Kender et al., 2018)(Kender et al.,
362 2018)(Kender et al., 2018).

363

364 After the 900 ka event, glacial-interglacial coupling in the nutrient upwelling index and climate
365 proxies supports the hypothesis that nutrient upwelling strength in the Bering Sea was controlled
366 by NPIW formation, modulated by ice sheet growth/sea level decline which followed quasi-100
367 kyr glacial cycles. Given that sea ice volumes remained higher during both glacials and
368 interglacials after the MPT, variability in sea ice seasonality is still considered to have played a
369 role in our upwelling nutrient record. However, continued closure of the Bering Strait in post-MPT
370 glacials may have promoted NPIW as the dominant mechanism for suppressing nutrient upwelling,
371 causing more prominent glacial-interglacial variability in the nutrient upwelling record. Further
372 model and high resolution CO_2 proxy reconstruction work is needed to better quantify the role of
373 NPIW expansion on the “saw-tooth” shape of post-MPT glacial cycles, as well as the significance
374 of regional changes on global ocean-atmosphere CO_2 exchanges.

375

376 Overall, we surmise that MPT sea ice dynamics controlled nutrient upwelling strength in
377 the Bering Sea and subarctic Pacific via two mechanisms: primarily through NPIW expansion
378 following sea-level modulated Bering Strait closure from ~ 0.9 Ma, which acted to suppress
379 regional upwelling during glacials as expressed in the LR04 global $\delta^{18}\text{O}$ stack. We also posit that
380 sea ice played a secondary role on the upwelling index through controlling seasonal primary
381 productivity and nutrient utilisation at the Bering slope, which caused higher frequency variability
382 in nutrient upwelling, particularly during sea ice expansion leading up to the 900 ka event.

383

384 **Acknowledgments, Samples, and Data**

385 We would like to thank the International Ocean Drilling Program for providing samples as well as
386 the Expedition 323 staff and crew of the JOIDES Resolution, and the curators at the Kochi Core
387 Centre. This research was part of a PhD project funded by Natural Environment Research Council
388 (NERC) Envision DTP, CASE funding from the British Geological Survey and NERC Isotope
389 Geosciences Facilities Steering Committee grant IP-1674-1116 (to SK). SW performed the sample

390 preparation, statistical analyses and led the writing of the manuscript. All authors assisted in
391 writing and contributed to interpretations on the manuscript. SK conceived the overall project and
392 isotope analyses were overseen by MJL and CR. We are also grateful to Dyke Andreasen and
393 Colin Carney from the University of California Santa Cruz as well as Christopher Kendrick and
394 Jack Lacey from the National Environmental Isotope Facility, for support with instrumentation
395 and sample preparation. All data needed to evaluate the conclusions in the paper are present in the
396 paper and/or the Supplementary Materials. Additional data related to this paper is available at
397 www.pangaea.de, or may be requested from the authors.

398 **References**

- 399 Aguilar-Islas, A. M., Hurst, M. P., Buck, K. N., Sohst, B., Smith, G. J., Lohan, M. C., &
400 Bruland, K. W. (2007). Micro- and macronutrients in the southeastern Bering Sea: Insight
401 into iron-replete and iron-depleted regimes. *Progress in Oceanography*, 73(2), 99–126.
402 <https://doi.org/10.1016/j.pcean.2006.12.002>
- 403 Aguilar-Islas, A. M., Rember, R. D., Mordy, C. W., & Wu, J. (2008). Sea ice-derived dissolved
404 iron and its potential influence on the spring algal bloom in the Bering Sea. *Geophysical*
405 *Research Letters*, 35(24), 10–14. <https://doi.org/10.1029/2008GL035736>
- 406 Aiello, I. W., & Ravelo, A. C. (2012). Evolution of marine sedimentation in the bering sea since
407 the pliocene. *Geosphere*, 8(6), 1231–1253. <https://doi.org/10.1130/GES00710.1>
- 408 Asahi, H., Kender, S., Ikehara, M., Sakamoto, T., Takahashi, K., Ravelo, a. C. C., ... Leng, M.
409 J. J. (2016). Orbital-scale benthic foraminiferal oxygen isotope stratigraphy at the northern
410 Bering Sea Slope Site U1343 (IODP Expedition 323) and its Pleistocene paleoceanographic
411 significance. *Deep-Sea Research Part II: Topical Studies in Oceanography*, 125–126, 66–
412 83. <https://doi.org/10.1016/j.dsr2.2014.01.004>
- 413 Billups, K., York, K., & Bradtmiller, L. I. (2018). Water Column Stratification in the Antarctic
414 Zone of the Southern Ocean During the Mid-Pleistocene Climate Transition.
415 *Paleoceanography and Paleoclimatology*, 33(5), 432–442.
416 <https://doi.org/10.1029/2018PA003327>
- 417 Brunelle, B. G., Sigman, D. M., Cook, M. S., Keigwin, L. D., Haug, G. H., Plessen, B., ...
418 Jaccard, S. L. (2007). Evidence from diatom-bound nitrogen isotopes for subarctic Pacific
419 stratification during the last ice age and a link to North Pacific denitrification changes.
420 *Paleoceanography*, 22(1), 1–17. <https://doi.org/10.1029/2005PA001205>
- 421 Chalk, T. B., Hain, M. P. M. P., Foster, G. L., Rohling, E. J., Badger, M. P. S., Cherry, S. G. S.
422 G. S. G., ... Wilson, P. A. P. A. P. A. (2017). Causes of ice age intensification across the
423 Mid-Pleistocene Transition. *Proceedings of the National Academy of Sciences*, 114(50),
424 201702143. <https://doi.org/10.1073/pnas.1702143114>
- 425 Clark, P. U., Archer, D., Pollard, D., Blum, J. D., Rial, J. A., Brovkin, V., ... Roy, M. (2006).
426 The middle Pleistocene transition: characteristics, mechanisms, and implications for long-
427 term changes in atmospheric pCO₂. *Quaternary Science Reviews*, 25(23–24), 3150–3184.
428 <https://doi.org/10.1016/j.quascirev.2006.07.008>
- 429 Clark, P. U., & Pollard, D. (1998). Origin of the middle Pleistocene transition by ice sheet

- 430 erosion of regolith. *Paleoceanography*, 13(1), 1–9. <https://doi.org/10.1029/97PA02660>
- 431 Crowley, T. J., & Hyde, W. T. (2008). Transient nature of late Pleistocene climate variability.
432 *Nature*, 456(7219), 226–230. <https://doi.org/10.1038/nature07365>
- 433 Detlef, H., Belt, S. T., Sosdian, S. M., Smik, L., Lear, C. H., Hall, I. R., ... Kender, S. (2018).
434 Sea ice dynamics across the Mid-Pleistocene transition in the Bering Sea. *Nature*
435 *Communications*, 9(1). <https://doi.org/10.1038/s41467-018-02845-5>
- 436 Detlef, H., Sosdian, S. M., Kender, S., Lear, C. H., & Hall, I. R. (2020). Multi-elemental
437 composition of authigenic carbonates in benthic foraminifera from the eastern Bering Sea
438 continental margin (International Ocean Discovery Program Site U1343). *Geochimica et*
439 *Cosmochimica Acta*, 268, 1–21. <https://doi.org/10.1016/j.gca.2019.09.025>
- 440 Elderfield, H., Ferretti, P., Greaves, M., Crowhurst, S. J., McCave, I. N., Hodell, D. a, &
441 Piotrowski, A. M. (2012). Evolution of ocean temperature. *Science*, 337(August), 704–709.
442 <https://doi.org/10.1594/PANGAEA.786205>
- 443 Galbraith, E. D., Kienast, M., Jaccard, S. L., Pedersen, T. F., Brunelle, B. D., Sigman, D. M., &
444 Kiefer, T. (2008). Consistent relationship between global climate and surface nitrate
445 utilization in the western subarctic Pacific throughout the last 500 ka. *Paleoceanography*,
446 23(2), 1–11. <https://doi.org/10.1029/2007PA001518>
- 447 Gildor, H., & Tziperman, E. (2001). A sea ice climate switch mechanism for the 100-kyr glacial
448 cycles. *Journal of Geophysical Research*, Vol. 106, p. 9117.
449 <https://doi.org/10.1029/1999JC000120>
- 450 Gray, W. R., Rae, J. W. B., Wills, R. C. J., Shevenell, A. E., Taylor, B., Burke, A., ... Lear, C.
451 H. (2018). Deglacial upwelling, productivity and CO2 outgassing in the North Pacific
452 Ocean. *Nature Geoscience*, 11(5), 340–344. <https://doi.org/10.1038/s41561-018-0108-6>
- 453 Hansell, D. A., Goering, J. J., Walsh, J. J., McRoy, C. P., Coachman, L. K., & Whitley, T. E.
454 (1989). Summer phytoplankton production and transport along the shelf break in the Bering
455 Sea. *Continental Shelf Research*, 9(12), 1085–1104. [https://doi.org/10.1016/0278-](https://doi.org/10.1016/0278-4343(89)90060-5)
456 [4343\(89\)90060-5](https://doi.org/10.1016/0278-4343(89)90060-5)
- 457 Heslop, D., Dekkers, M. J., & Langereis, C. G. (2002). Timing and structure of the mid-
458 Pleistocene transition: Records from the loess deposits of northern China.
459 *Palaeogeography, Palaeoclimatology, Palaeoecology*, 185(1–2), 133–143.
460 [https://doi.org/10.1016/S0031-0182\(02\)00282-1](https://doi.org/10.1016/S0031-0182(02)00282-1)
- 461 Hönisch, B., Hemming, G. N., Archer, D., Siddall, M., & McManus, J. F. (2009). Atmospheric
462 Carbon Dioxide Concentration Across the Mid-Pleistocene Transition. *Science*, 324(5934),
463 1551–1554. <https://doi.org/10.1126/science.1229223>
- 464 Jouzel, J., Masson-Delmotte, V., Cattani, O., Dreyfus, G., Falourd, S., Hoffmann, G., ... Wolff,
465 E. W. (2007). Orbital and Millennial Antarctic Climate Variability over the Past 800,000
466 years. *Science*, 317(August), 793–796. <https://doi.org/10.1126/science.1141038>
- 467 Kanematsu, Y., Takahashi, K., Kim, S., Asahi, H., & Khim, B. K. (2013). Changes in biogenic
468 opal productivity with Milankovitch cycles during the last 1.3Ma at IODP Expedition 323
469 Sites U1341, U1343, and U1345 in the Bering Sea. *Quaternary International*, 310, 213–
470 220. <https://doi.org/10.1016/j.quaint.2013.06.003>

- 471 Kender, S., Ravelo, A. C., Worne, S., Swann, G. E. A., Leng, M. J., Asahi, H., ... Hall, I. R.
472 (2018). Closure of the Bering Strait caused Mid-Pleistocene Transition cooling. *Nature*
473 *Communications*, 9(5386). <https://doi.org/10.1038/s41467-018-07828-0>
- 474 Kim, S., & Khim, B. K. (2016). Reconstruction of nitrate utilization rate change based on
475 diatom-bound nitrogen isotope values in the central slope area of the Bering sea during the
476 early pleistocene (2.4–1.25 Ma). *Ocean and Polar Research*, 38(3), 195–207.
477 <https://doi.org/10.4217/OPR.2016.38.3.195>
- 478 Kim, S., Khim, B. K., Ikehara, M., & Takahashi, K. (2017). Relationship between $\delta^{15}\text{N}$ values
479 of bulk sediments and total organic carbon concentration in response to orbital-scale
480 biogenic opal production in the Bering slope area over the last 600 kyrs. *Quaternary*
481 *International*, 459(3), 144–152. <https://doi.org/10.1016/j.quaint.2017.05.041>
- 482 Kim, S., Takahashi, K., Khim, B. K., Kanematsu, Y., Asahi, H., & Ravelo, A. C. (2014).
483 Biogenic opal production changes during the Mid-Pleistocene Transition in the Bering Sea
484 (IODP Expedition 323 Site U1343). *Quaternary Research (United States)*, 81(1), 151–157.
485 <https://doi.org/10.1016/j.yqres.2013.10.001>
- 486 Knudson, K. P., & Ravelo, A. C. (2015a). Enhanced subarctic Pacific stratification and nutrient
487 utilization during glacials over the last 1.2 Myr. *Geophysical Research Letters*, 42(22),
488 9870–9879. <https://doi.org/10.1002/2015GL066317>
- 489 Knudson, K. P., & Ravelo, A. C. (2015b). North Pacific Intermediate Water circulation enhanced
490 by the closure of the Bering Strait. *Paleoceanography*, 30(10), 1287–1304.
491 <https://doi.org/10.1002/2015PA002840>
- 492 Lisiecki, L. E., & Raymo, M. E. (2005). A Pliocene-Pleistocene stack of 57 globally distributed
493 benthic $\delta^{18}\text{O}$ records. *Paleoceanography*, 20(1), 1–17.
494 <https://doi.org/10.1029/2004PA001071>
- 495 Liu, Z., Altabet, M. A., & Herbert, T. D. (2005). Glacial-interglacial modulation of eastern
496 tropical North Pacific denitrification over the last 1.8-Myr. *Geophysical Research Letters*,
497 32(23), 1–4. <https://doi.org/10.1029/2005GL024439>
- 498 Liu, Z., & Herbert, T. D. (2004). High-latitude influence on the eastern equatorial Pacific climate
499 in the early Pleistocene epoch. *Nature*, 430(July), 560–564.
500 <https://doi.org/10.1038/nature02295.1>
- 501 Lüthi, D., Le Floch, M., Bereiter, B., Blunier, T., Barnola, J. M., Siegenthaler, U., ... Stocker, T.
502 F. (2008). High-resolution carbon dioxide concentration record 650,000–800,000 years
503 before present. *Nature*, 453(7193), 379–382. <https://doi.org/10.1038/nature06949>
- 504 Marlow, J. R., Lange, C. B., Wefer, G., & Rosell-Mele, a. (2000). Upwelling intensification as
505 part of the Pliocene-Pleistocene climate transition. *Science*, 290(5500), 2288–2291.
506 <https://doi.org/10.1126/science.290.5500.2288>
- 507 Martínez-García, A., Rosell-Melé, A., Jaccard, S. L., Geibert, W., Sigman, D. M., & Haug, G. H.
508 (2011). Southern Ocean dust-climate coupling over the past four million years. *Nature*,
509 476(7360), 312–315. <https://doi.org/10.1038/nature10310>
- 510 Martínez-García, A., Rosell-Melé, A., McClymont, E. L., Gersonde, R., & Haug, G. H. (2010).
511 Subpolar Link to Emergence of the Modern Equatorial Pacific Cold Tongue. *Science*,

- 512 328(5985), 1550–1553.
- 513 McClymont, E. L., & Rosell-Melé, A. (2005). Links between the onset of modern Walker
514 circulation and the mid-Pleistocene climate transition. *Geology*, 33(5), 389–392.
515 <https://doi.org/10.1130/G21292.1>
- 516 McClymont, E. L., Rosell-Melé, A., Haug, G. H., & Lloyd, J. M. (2008). Expansion of subarctic
517 water masses in the North Atlantic and Pacific oceans and implications for mid-Pleistocene
518 ice sheet growth. *Paleoceanography*, 23(4), 1–12. <https://doi.org/10.1029/2008PA001622>
- 519 McClymont, E. L., Sosdian, S. M., Rosell-Melé, A., & Rosenthal, Y. (2013). Pleistocene sea-
520 surface temperature evolution: Early cooling, delayed glacial intensification, and
521 implications for the mid-Pleistocene climate transition. *Earth-Science Reviews*, 123, 173–
522 193. <https://doi.org/10.1016/j.earscirev.2013.04.006>
- 523 Pena, L. D., & Goldstein, S. L. (2014). Thermohaline circulation crisis and impacts during the
524 mid-Pleistocene transition. *Science*, 345(6194), 318–322.
525 <https://doi.org/10.1126/science.1249770>
- 526 Pollard, D., & DeConto, R. M. (2009). Modelling West Antarctic ice sheet growth and collapse
527 through the past five million years. *Nature*, 458(7236), 329–332.
528 <https://doi.org/10.1038/nature07809>
- 529 Rae, J. W. B., Sarnthein, M., Foster, G. L., Ridgwell, A., Grootes, P. M., & Elliott, T. (2014).
530 Deep water formation in the North Pacific and deglacial CO₂ rise. *Paleoceanography*, 29,
531 1–23. <https://doi.org/10.1002/2013PA002570>.Received
- 532 Raymo, M. E. (1997). The timing of major climate terminations. *Paleoceanography*, 12(4), 577–
533 585. <https://doi.org/10.1029/97PA01169>
- 534 Raymo, M. E., Lisiecki, L. E., Nisancioglu, K. H., Hemispheres, S., & Instead, O. (2006). Plio-
535 Pleistocene Ice Volume, Antarctic Climate, and the Global δ¹⁸O Record. *Nature*, 313(July),
536 492–495. <https://doi.org/10.1126/science.1123296>
- 537 Rodríguez-Sanz, L., Graham Mortyn, P., Martínez-García, A., Rosell-Melé, A., & Hall, I. R.
538 (2012). Glacial Southern Ocean freshening at the onset of the Middle Pleistocene Climate
539 Transition. *Earth and Planetary Science Letters*, 345–348, 194–202.
540 <https://doi.org/10.1016/j.epsl.2012.06.016>
- 541 Schmieder, F., Von Dobeneck, T., & Bleil, U. (2000). The Mid-Pleistocene climate transition as
542 documented in the deep South Atlantic Ocean: Initiation, interim state and terminal event.
543 *Earth and Planetary Science Letters*, 179(3–4), 539–549. [https://doi.org/10.1016/S0012-821X\(00\)00143-6](https://doi.org/10.1016/S0012-821X(00)00143-6)
- 544
- 545 Sexton, P. F., & Barker, S. (2012). Onset of “Pacific-style” deep-sea sedimentary carbonate
546 cycles at the mid-Pleistocene transition. *Earth and Planetary Science Letters*, 321–322, 81–
547 94. <https://doi.org/10.1016/j.epsl.2011.12.043>
- 548 Sigman, D. M., Hain, M. P., & Haug, G. H. (2010). The polar ocean and glacial cycles in
549 atmospheric CO₂ concentration. *Nature*, 466(7302), 47–55.
550 <https://doi.org/10.1038/nature09149>
- 551 Snyder, C. W. (2016). Evolution of global temperature over the past two million years. *Nature*,
552 538(7624), 226–228. <https://doi.org/10.1038/nature19798>

- 553 Stabeno, P. J., Schumacher, J. D., & Ohtani, K. (1999). The physical oceanography of the Bering
554 Sea. *Dynamics of the Bering Sea*, 1–60. Retrieved from
555 ftp://128.112.177.15/pub/edac/bering_sea/Stabeno_1999_bering_sea.pdf
- 556 Stroynowski, Z., Abrantes, F., & Bruno, E. (2017). The response of the Bering Sea Gateway
557 during the Mid-Pleistocene Transition. *Palaeogeography, Palaeoclimatology,*
558 *Palaeoecology*, 485(March), 974–985. <https://doi.org/10.1016/j.palaeo.2017.08.023>
- 559 Takahashi, K., Ravelo, A. C., Alvarez Zarikian, C. A., & Scientists, E. 323. (2011). Site U1343.
560 *Proceedings of the IODP*, 323, 323. <https://doi.org/10.2204/iodp.proc.323.107.2011>
- 561 Takeda, S. (2011). Iron and Phytoplankton Growth in the Subarctic North Pacific. *Aqua-*
562 *BioScience Monographs*, 4(2), 41–93. <https://doi.org/10.5047/absm.2011.00402.0041>
- 563 Talley, L. D. (1993). Distribution and Formation of North Pacific Intermediate Water. *Journal of*
564 *Physical Oceanography*, 23, 517–537.
- 565 Teraishi, A., Suto, I., Onodera, J., & Takahashi, K. (2016). Diatom, silicoflagellate and ebridian
566 biostratigraphy and paleoceanography in IODP 323 Hole U1343E at the Bering slope site.
567 *Deep-Sea Research Part II: Topical Studies in Oceanography*, 125–126, 18–28.
568 <https://doi.org/10.1016/j.dsr2.2013.03.026>
- 569 Worne, S., Kender, S., Swann, G. E. A., Leng, M. J., & Ravelo, A. C. (2019). Coupled climate
570 and subarctic Pacific nutrient upwelling over the last 850, 000 years. *Earth and Planetary*
571 *Science Letters*, 522, 87–97.
- 572 Yasuda, I. (1997). The origin of the North Pacific Intermediate Water. *Journal of Geophysical*
573 *Research: Oceans*, 102(C1), 893–909. <https://doi.org/10.1029/96jc02938>
- 574

575 **Supplementary Information**

576

577

Supplementary Table 1 New age-depth tie points for Site U1343, building on Worne et al. (2019).

Depth (CCSF – A) (m)	Age (ka)
0.96	10.15
14.23	57.38
36.72	131.41
48.03	181.46
59.73	219.06
68.72	242.57
79.52	279.96
96.24	335.14
114.56	396.17
119.35	424.39
129.90	480.93
145.02	512.78
152.01	545.32
161.63	580.48
173.39	621.39
174.57	641.03
184.09	700.03
188.27	725.84
191.58	753.63
203.57	790.75
209.04	812.86
227.39	865.95
238.34	917.46
254.16	959.01
266.14	983.50
272.57	1002.99
282.73	1031.59
296.57	1062.96
318.81	1124.99
336.91	1190.47

578